FAR-ULTRAVIOLET MAPPING OF THE CYGNUS LOOP WITH THE *VOYAGER 2* ULTRAVIOLET SPECTROMETER

WILLIAM P. BLAIR, KNOX S. LONG,[1] AND OLAF VANCURA
Department of Physics and Astronomy, The Johns Hopkins University, Charles & 34th Streets, Baltimore, MD 21218

AND

J. B. HOLBERG
Lunar and Planetary Laboratory, Gould-Simpson Building, University of Arizona, Tucson, AZ 85721

ABSTRACT

We report far-ultraviolet maps of the Cygnus Loop made using spectroscopic data from the *Voyager 2* Ultraviolet Spectrometer. Emission line features at ~980 and ~1035 Å dominate the 500–1700 Å spectra of the Cygnus Loop as observed with *Voyager*, and we have generated maps in the light of these two features. We have compared the 980 and 1035 Å maps with X-ray and optical images of the Cygnus Loop that have been sampled in the same manner. From this comparison, it is clear that the 980 Å feature arises mainly from regions of bright optical emission, whereas the 1035 Å emission more closely resembles the X-ray emission. This general impression can be confirmed by inspection of the spectra as a function of position. Spectra extracted from positions corresponding to the primary shock front show the 1035 Å feature to be relatively strong, while the 980 Å feature is brighter when substantial optical emission is present within the aperture. This distribution is consistent with the idea that the 980 Å feature is dominated by C III λ977 while the 1035 Å feature is dominated by O VI $\lambda\lambda$1032, 1038. Luminosities of the Cygnus Loop in C III and O VI are ~2.7×10^{36} ergs s^{-1} and ~4.6×10^{36} ergs s^{-1}, respectively. The ubiquity of O VI emission implies that shocks with velocity greater than 160 km s^{-1} are widespread throughout the Cygnus Loop.

Subject headings: nebulae: individual (Cygnus Loop) — nebulae: supernova remnants — shock waves — ultraviolet: spectra

1. INTRODUCTION AND BACKGROUND

The Cygnus Loop is generally considered to be the proto-typical "middle-aged" supernova remnant (SNR). It is probably in the later stages of adiabatic expansion or just entering the radiative phase of its evolution. The proper-motion measurements coupled with observed shock velocities imply distances of 700–770 pc to the remnant (see Fesen, Blair, & Kirshner 1982; Hester, Raymond, & Danielson 1986). Published values vary up and down from this distance by a factor of 2 (see Kirshner & Taylor 1976; Braun & Strom 1986; Sakhibov & Smirnov 1983). At 770 pc the ~3° × 4° angular extent of the object corresponds to a linear dimension of ~40 × 54 pc. Because of its proximity, low-extinction $E(B-V) = 0.08$; (Miller 1974; Fesen et al. 1982), and well-resolved filamentary structure, the Cygnus Loop is an object of great importance to those interested in shock waves because it provides a forum for investigating both the global properties and the details of the shock wave/interstellar medium (ISM) interaction.

The passage of a blast wave through an inhomogeneous region of the ISM manifests itself in different ways. The main blast wave travels through the low-density, large filling-factor portion of the ISM, heating it to millions of degrees and causing thermal X-ray emission. As the blast wave encounters density enhancements (i.e., clouds), it both sweeps around these clouds and drives slower shocks into the clouds (see McKee & Ostriker 1977); bright optical and ultraviolet emission arises in the cooling and recombination zones of these secondary shocks (see Raymond et al. 1980, 1981; Benvenuti, Dopita, &

D'Odorico 1980; Raymond et al. 1983; 1988). If the cloud/shock interaction has taken place recently, the shock will not have had time to form a complete cooling and recombination zone. Spectra of these incomplete or nonsteady flow shocks will show enhanced high-ionization line strengths. In the Cygnus Loop many optical filaments appear overly strong in [O III] and are thought to be due to this phenomenon (Fesen et al. 1982; Hester, Parker, & Dufour 1983).

On the largest scales, optical, radio, infrared, and X-ray maps of the Cygnus Loop all show a limb-brightened morphology (Ku et al. 1984; Charles, Kahn, & McKee 1985; Braun & Strom 1986; Fesen et al. 1982; Keen et al. 1973). X-ray emission extends radially outward from the bright optical filaments to a complex string of faint optical filaments dominated by hydrogen Balmer-line emission (Raymond et al. 1983, hereafter RBFG; Fesen & Itoh 1985; Hester, Raymond, & Danielson 1986). These faint filaments, primarily in the NE, N, and W sections of the Cygnus Loop, are thought to demark the leading edge of the blast wave as it encounters partially neutral ISM (see Chevalier, Kirshner, & Raymond 1980). Such shocks are called nonradiative shocks because radiative losses are insignificant on the dynamical time scale of the shock front (McKee & Hollenbach 1980). Although exceedingly faint optically, observations with the *International Ultraviolet Explorer* satellite (*IUE*) indicate the high-ionization UV line intensities in these filaments are comparable to those of the bright optical filaments and imply ~200 km s^{-1} shock velocities (see RBFG). This is much lower than the ~400 km s^{-1} velocities typically inferred from the X-ray emission.

Recent investigations have used multiwavelength data to elaborate further on the details of the shock wave/

[1] Postal address: Space Telescope Science Institute, 3700 San Martin Drive, Baltimore, MD 21218.

inhomogeneous ISM picture of the Cygnus Loop. Hester & Cox (1986) and Teske (1990) have applied optical and X-ray imaging data to this problem, constraining cloud sizes and physical conditions and placing limits on the importance of cloudlet evaporation in the postshock gas. Raymond et al. (1988) have used optical/UV spectroscopy to investigate a filament in transition to becoming fully radiative, concluding that thermal pressure may not be the dominant pressure source in SNR filaments. Boulares & Cox (1988) subsequently have elaborated on the possible importance of cosmic rays in the dynamics of SNR filaments.

The purpose of the current paper is to study the global aspects of the ultraviolet emission from the Cygnus Loop. The Cygnus Loop has been a favorite target of the *IUE* satellite, but only a small sample of the SNR's filaments have been studied during the 13 yr of *IUE* operations. Carruthers & Page (1976) report low-resolution, broad-band UV images covering a portion of the Cygnus Loop obtained with an electrographic Schmidt camera on *Apollo 16*. However, the overall morphology of the Cygnus Loop in key ultraviolet emission lines has never been measured. Also, it is important to extend wavelength coverage for SNRs down to the practical limit at 912 Å. The 912–1200 Å region is full of many potential plasma diagnostics, from the H_2 Lyman and Werner bands to O VI $\lambda\lambda 1032$, 1038 to the higher members of the Lyman series of hydrogen. For example, the nonradiative shocks in the Cygnus Loop should be prodigious emitters of O VI $\lambda\lambda 1032$, 1038, which peaks (in ionization equilibrium) in regions with temperatures near 300,000 K. The O VI lines are a crucial diagnostic because they come from a temperature region intermediate between the X-ray gas and that sampled by the other UV lines ($\leq 100,000$ K). For nonradiative shocks, the O VI line emission discriminates between various models of electron-ion equilibration in the postshock gas (see RBFG). Also, if material is evaporated from the shocked clouds (see McKee, Cowie, & Ostriker 1978), one would expect O VI emission from relatively slow shocks as well. This spectral region also provides additional lines of C, N, O, S, and Si.

Very few observations of the 912–1200 Å region have been reported. O VI was seen in absorption when *Copernicus* observed stars behind the Vela SNR (Jenkins, Silk, & Wallerstein 1976), but little is known about its spatial distribution. Shemansky, Sandel, & Broadfoot (1979) discuss data from three isolated regions in the Cygnus Loop obtained with the *Voyager 2* UVS in 1978. These observations were sufficient to demonstrate that line intensity variations were present in the far-UV spectrum of the Cygnus Loop, but the ~30 Å effective resolution and uncertainties in the models available at that time hindered the unambiguous identification of some of the emission lines present in the spectra.

A much larger body of *Voyager* UVS data exists, including observations obtained in 1979–1980 that cover the entire remnant. In this paper we present maps of the Cygnus Loop in the light of two prominent peaks in *Voyager's* spectral range that have been derived from these observations and compare this global perspective of the UV emission with optical and X-ray data. In § 2 we discuss the observations and reductions. In § 3 we present the UV maps of the Cygnus Loop made from the *Voyager* data and compare them with X-ray and optical data on the Cygnus Loop. We also show spectra extracted from various portions of the maps. In § 4 we discuss the interpretation of these data and identify the primary emission lines that make up the map emissions. Finally, § 5 contains a brief summary.

2. OBSERVATIONS

The *Voyager 2* UVS is an objective grating spectrometer employing a microchannel plate intensifier and a 126 channel self-scanned array detector. The dispersion is 9.3 Å channel^{-1} with a spectral resolution of 15 and 30 Å for point and extended sources, respectively. The field of view (FOV) is a $0°.10 \times 0°.87$ aperture projected on the sky. Additional information concerning the UVS instrumentation may be found in Broadfoot et al. (1977, 1981). The *Voyager* UVS was designed to observe planetary atmospheres but has also been very useful in obtaining low-resolution 500–1700 Å spectra of many astronomical sources. Among these interplanetary cruise observations was a 2 month series of observations of the Cygnus Loop made with the *Voyager 2* UVS in 1979–1980.

The *Voyager* mapping of the Cygnus Loop was accomplished using a series of 21 nebular pointings and two background pointings as shown in Figure 1 (Plate 4). For all of the mapping observations, the long direction of the aperture was oriented 49° E of N. As a result, the resolution of the maps we construct below differs in two orthogonal directions. As shown in the figure, the aperture was oriented nearly perpendicular to the strong filamentary optical emission in the NE and more or less parallel to the shock front in the NW. Positions intermediate to each nominal aperture position were sampled through the motion of the FOV with respect to the sky. This motion was a combination of the limit cycle motion and a slow systematic drift of the FOV with respect to inertial coordinates. Limit cycle motion arises because the spacecraft's attitude control system permits the spacecraft to drift within a dead band, with quasi-periodic (~25 minute) motions of ~0°.3 amplitude along the principal axes of the UVS slit. The systematic drift of the FOV with respect to the sky arises from the necessity of the fixed high-gain antenna to track the Earth and results in a drift averaging approximately 0°.1 per day. The net effect of these two motions was to provide nearly complete coverage of the region defined by the dashed line in Figure 1. In all, approximately 15,500 spectra were obtained, including about 2000 from sky background regions (see Table 1). During the period in which the Cygnus Loop was being observed nearly all UVS spectra were obtained in the CR4 data mode, in which one complete spectrum was returned every 192 s. Data obtained in GS3 mode (one spectrum every 3.84 s) were treated separately and normalized to 192 s. Attitude control system error signals were used to compute pointing location as a function of time for each individual spectrum.

Several instrumental corrections have been applied to these data, including a flat field or "fixed pattern noise" correction, dark and sky background subtraction, and an instrumental scattering correction. The rationale and details of these corrections are discussed by Holberg (1986, 1991). The dominant component of the sky background in these data is due to line emission, primarily H I Lyα but also higher Lyman lines and He I $\lambda 584$, from the interplanetary medium (IPM). This "foreground" emission arises from the scattering of solar line emission by neutral H and He within the IPM. The interplanetary emission component varies in direct proportion to the intensity of the illuminating solar lines (see Shemansky, Judge, & Jessen 1984), which in turn are a function of solar activity and the rotation of active solar regions into the hemisphere containing *Voyager 2*. Variations of 50% were observed in the Lyα intensity over the 2 month observing period.

The variable Lyα made it necessary to perform a time-dependent background correction for the Cygnus Loop data. This was accomplished using the previously mentioned sky
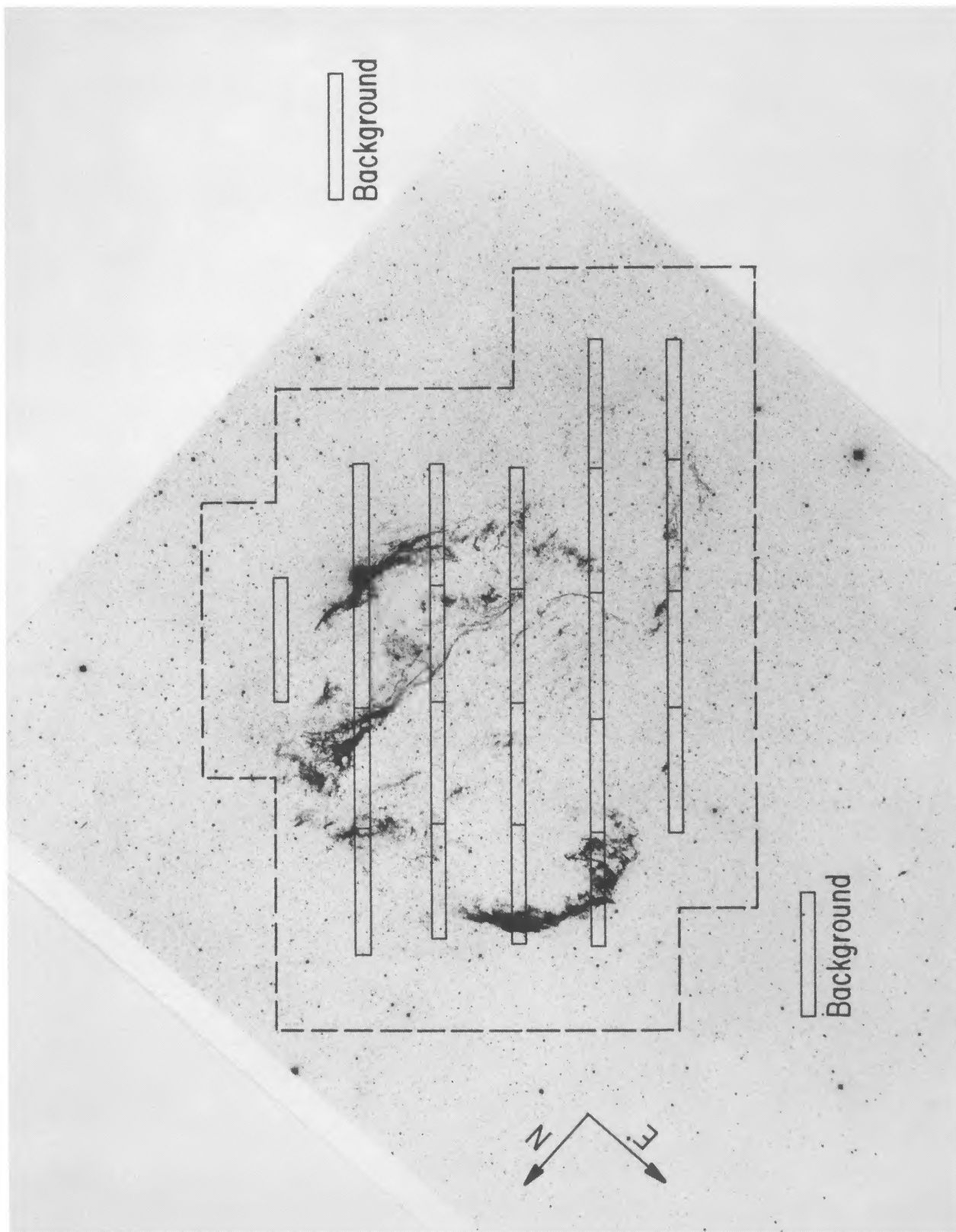
PLATE 4

Fig. 1.—Cygnus Loop from the red Palomar Observatory Sky Survey print is shown with the grid of nominal UVS FOV positions used for mapping the nebula overlaid. Oscillations of the spacecraft during the observations permitted nearly complete mapping of the region enclosed by the dashed line. Nominal background positions are also shown. For scale, the *Voyager* FOV is 0.1×0.87.

Blair et al. (see 374, 203)

TABLE 1

Voyager 2 Cygnus Loop Mapping Parameters

Observation Number	Location[a]		Initial Time[b] (DOY/SCET)	Duration[c] (hr)	Data Mode[d] (CR4/GS3)
	α (1950)	δ (1950)			
1	313°.78	31°.055	331/19:42:10	29.3	418/835
2	313.21	30.476	333/01:00:31	38.0	486/1299
3	312.62	29.9	334/15:00:20	72.0	783/0
4	313.35	31.388	337/15:00:52	27.4	798/799
5	312.77	30.8	338/18:24:27	27.7	303/0
6	312.18	30.223	341/02:52:07	20.8	207/3100
7	312.93	31.721	341/23:40:52	63.3	1012/0
8	312.33	31.125	344/15:00:32	32.5	317/0
9	311.74	30.546	345/23:30:25	24.0	312/0
10	312.50	32.055	347/23:30:47	24.0	513/0
11	311.89	31.499	348/18:09:01	71.2	647/0
12	311.29	30.869	351/17:20:36	45.2	543/0
13[e]	315.25	30.50	353/23:09:05	161.9	1687/0
14	310.85	31.19	360/17:00:33	22.0	354/0
15	313.65	30.15	361/15:00:26	24.0	313/0
16	313.06	29.58	362/15:00:20	120.0	1418/0
17	312.04	29.32	002/22:51:52	40.1	528/0
18	311.60	29.64	004/15:00:18	72.0	937/0
19	311.16	29.96	007/15:00:18	24.0	381/0
20	310.71	30.28	008/15:00:19	24.0	473/0
21	312.48	28.99	011/06:13:29	87.8	1332/0
22	311.46	28.74	014/22:00:20	17.0	114/0
23[e]	308.80	28.50	015/15:00:26	29.2	341/0
			017/01:18:20	37.6	926/0
24[e]	311.89	28.41	036/21:07:16	21.0	338/0
Totals				1156.0	15481/6033

[a] Nominal target coordinates for each observation.

[b] DOY/SCET (day of year/spacecraft event time) gives beginning time of each observation.

[c] Duration of each observation in hours.

[d] Number of spectra obtained in each data mode: CR4 = 192 s/spectrum, GS3 = 3.84 s/spectrum.

[e] Sky background pointings.

background data to define an instrumental dark count spectrum and an IPM emission-line template spectrum which could be scaled to match the Lyα line in each Cygnus Loop spectrum. (Decomposition of sky background spectra is described by Holberg 1986). The characteristic dark count spectrum is produced primarily by γ-radiation from the radioactive thermal generators which power the spacecraft, and has a value of $\sim 2.5 \times 10^{-2}$ counts s^{-1} channel^{-1}. This component was subtracted directly from the data. The interplanetary emission-line component was removed by scaling, as function of time, the Lyα feature in the template IPM spectrum to the observed brightness of the Lyα feature in the Cygnus Loop data. The primary assumption in doing this is that the Lyα intensities are due entirely to the IPM. This is not strictly true, as the Cygnus Loop spectra appear to contain an additional emission line ~ 20 Å longward of Lyα (presumably NV λ1240) and may well contain intrinsic Lyα emission as well. However, any intrinsic component would be strongly attenuated by resonant scattering in the ISM.

Following the subtraction of the dark count and IPM backgrounds, a correction for instrumental scattering was applied. This is a standard *Voyager* data reduction procedure which involves applying a 126 × 126 matrix operator that corrects the observed signal in channel *i* for the scattered contribution from channel *j*. Descattering is discussed in more detail by Holberg (1986).

3. EXTRACTION OF MAPS AND SPECTRA

Binning all of the spectra together produces the global Cygnus Loop spectrum shown in Figure 2. Two peaks at ~ 980 and ~ 1035 Å dominate this spectrum. Interstellar hydrogen cuts off any emission below 912 Å, and the *Voyager* sensitivity drops dramatically above ~ 1250 Å, strongly attenuating lines normally seen in the *IUE* spectral range. These two peaks are present in all of the individual spectra that have significant signal, indicating that the emission in these features is both ubiquitous and variable in the Cygnus Loop. These two emission peaks have thus been chosen for producing spatial maps of the Cygnus Loop. As discussed in § 4, comparison with shock model calculations (see Hartigan, Raymond & Hartmann 1987) suggests that C III λ977 and O VI λλ1032, 1038 are the dominant constituents of the 980 and 1035 Å peaks.

The individual spectra have been combined in the following manner in preparation for creating spatial maps. We created a spatial grid with 77 × 100 grid points of 0°.05 extent covering the region from R.A. (1950) = 310° to 314°.5 and Decl. (1950) = +28° to +33°. Individual spectra were placed into a box in the grid when the coordinates of the center of the *Voyager* FOV were within the box. This method of binning oversamples the spatial resolution of the *Voyager* UVS. However, with no a priori knowledge of where the emission is entering the *Voyager* aperture, placing all of the emission at the center provides a convenient representation for compari-
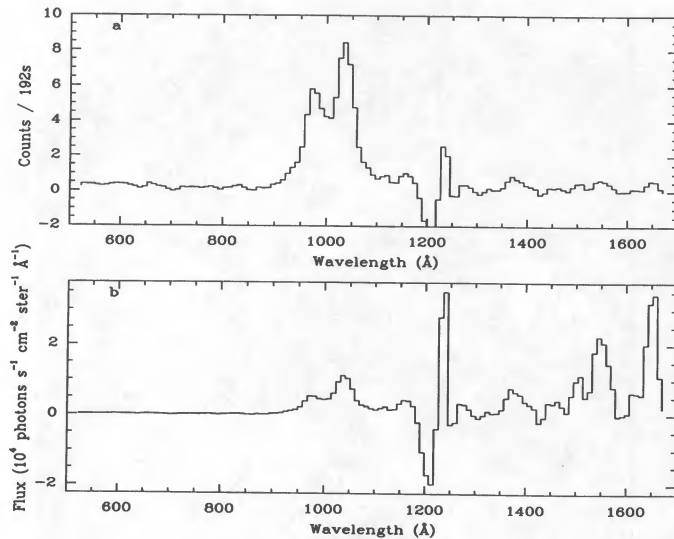
FIG. 2.—Globally averaged spectra of the Cygnus Loop as seen by the *Voyager* UVS. (*a*) Reduced summed Cygnus Loop mapping data after background and scattering corrections, normalized to the count rate per 192 s, which is the exposure time for a single spectrum. This is the average of nearly 14,000 individual spectra. Because of variations of the interplanetary Lyα component at 1216 Å, the subtraction of this feature has left a residual. Note the two main peaks centered at 980 and 1035 Å. (*b*) Same spectrum after application of the standard UVS flux calibration (Holberg et al. 1982). Because of attenuation of the UVS sensitivity longward of 1200 Å, the accuracy of measurements in this region are more uncertain. However, the feature at 1550 Å is due to C IV, and the 1650 Å feature may be a blend of He II and O III], although it appears to be too narrow.

FIG. 3.—Cygnus Loop grid showing time coverage as a function of spatial position in the map. The binning procedure causes some apparent holes in the coverage. Some bins contain as few as one 192 s spectrum, while others contain as many as 25 spectra. White grid points are regions of higher time coverage. Note the substantial coverage in the SE where the emission is quite faint.

son with other data sets (see below). This method of binning also creates apparent "holes" in the spatial coverage since some bins remained empty (i.e., had no FOV centers within their spatial coverage range) even though the region may have been technically sampled. Figure 3 shows a time coverage map and demonstrates the nonuniformity of the sampling. The spectra in each bin were summed and normalized to the sampling rate of 192 s. These normalized spectra form the basis for the monochromatic maps described below.

Maps of the 980 and 1035 Å emission were created by writing a computer program that, for each grid point, calculated the total number of counts in specified channel ranges from the normalized *Voyager* spectra. We chose channel ranges corresponding to the peak and far wing of each profile; 47–51 for the 980 Å feature and 56–60 for the 1035 Å feature. This was done to avoid the confused region between the emission peaks. The extended source point spread function (see Broadfoot et al. 1981) is narrow enough that no significant contamination of the maps should occur, assuming the emission peaks are dominated by emission features close to the observed centers of each peak. This is not a bad assumption where the emission peaks are strong (see below), but blending with other emission lines may be significant where one of the features is weak. Displaying the summed counts as a function of spatial position produces the maps shown in the left panels of Figure 4 (Plate 5).

Inspection of the maps show that there is considerable variation in the strength of both emission features and that the relative intensities of the features also vary as a function of position. The 980 Å map is brightest on the NW side of the remnant, while the 1035 Å map has a "hot spot" in the N and

is also bright on the NW and W sides of the SNR. At first, this seems quite at odds with the distribution of bright optical and X-ray emission, but sampling effects of the long, narrow *Voyager* aperture and the binning scheme we have used affect this comparison. The bright patch on the E side of the maps is not a star, but rather a bright patch of SNR emission "circularized" by sampling effects (see Fig. 3).

To test the effects of slit sampling and binning, we have obtained digitized X-ray and optical data on the Cygnus Loop and sampled them as if *Voyager* had observed in these wavelength bands. The X-ray data used was the *Einstein* IPC map (Ku et al. 1984) as reprocessed by Seward (1990). The optical data were provided by Ted Gull of NASA/GSFC, including [O III] λ5007 and 4200 Å continuum plates. These plates were obtained with a Carnegie Image Tube and 300 mm Nikon lens (see Parker, Gull, & Kirshner 1979) and include a 6° region centered on the Cygnus Loop. These plates were digitized into 2048 × 2048 pixels using the PDS machine at NASA/GSFC by Mike Greason. Hence, both X-ray and optical data sets had much finer initial spatial resolution than even the small dimension of the *Voyager* aperture. The 4200 Å continuum exposure was aligned and subtracted from the [O III] image to remove stars to first order. The resulting image was aligned to the *Voyager* data using the SAO star positions in the field. This was accomplished with IRAF on a Sun 386i workstation at Johns Hopkins.
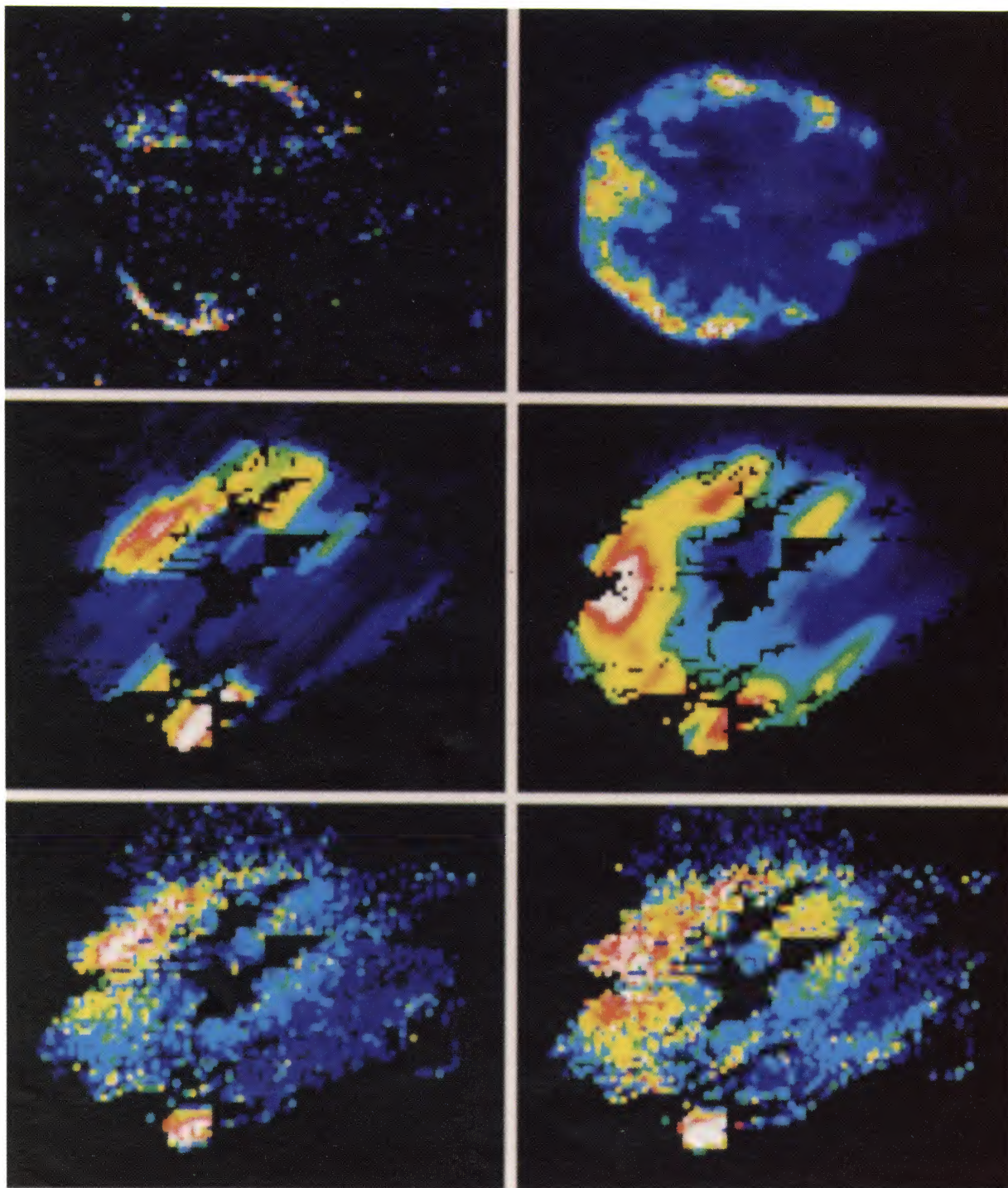
PLATE 5

Fig. 4.—Panels on the left show the *Voyager* maps of the Cygnus Loop as seen in (*top*) 980 Å emission and (*bottom*) 1035 Å emission. Panels on the right show (*top*) optical [O III] emission and (*bottom*) *Einstein* X-ray data binned into 0.05 bins and aligned with the *Voyager* maps. The center panels show how the [O III] and X-ray data would appear if sampled in the same way as the *Voyager* data. Note the general similarity in appearance of the 980 Å map and the [O III] data, as well as the 1035 Å map and the X-ray data.
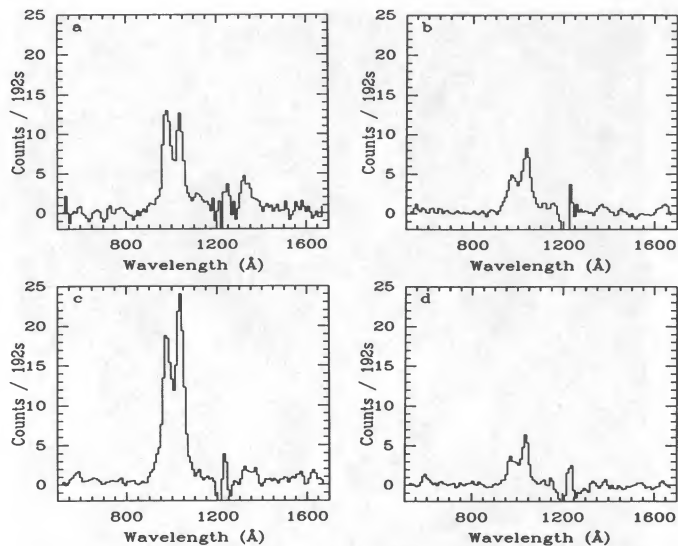
Blair et al. (see 374, 205)

FIG. 5.—Representative spectra extracted from four regions of the Cygnus Loop (see Fig. 6). Spectra are shown with the same vertical scaling and normalized to counts per 192 s, so both intrinsic and relative line intensity variations can be seen.

FIG. 6.—Black and white presentation of the 1035 Å map with overlay showing spectral regions extracted and shown in Fig. 5.

We wrote a computer program to pass a *Voyager*-like false aperture over these data to sample them as if observed by *Voyager*. The X-ray and optical data were binned into our standard grid and are shown in the central panels of Figure 4. For comparison the right-hand panels in Figure 4 show the optical and X-ray data binned to 0°.05 pixels but without smearing. Comparison of the smeared and unsmeared data in Figure 4 makes it clear that many of the brightness variations seen in the *Voyager* maps are due to the extent to which the FOV was filled with extended emission (see the NW portion of the [O III] maps). It is also clear that there is a great deal of similarity in the appearance of the 980 Å map and the smeared [O III] optical data, and between the 1035 Å map and the smeared X-ray emission. The 1035 Å feature thus appears to be associated with hotter gas than the 980 Å feature.

In order to emphasize this last point, we have extracted representative spectra of various regions of the Cygnus Loop, as shown in Figure 5. The regions of the Cygnus Loop from which the spectra were extracted are indicated on Figure 6, which is a black and white version of the 1035 Å map. Table 2 lists the actual coordinates for the binning regions depicted in Figure 6. These are the boundaries within which the center of the FOV was located, so the actual region represented by each spectrum is larger than that shown, especially in the NE to SW direction. Figure 5a shows the spectrum from the NW part of the Loop. It is centered on a bright region of optical emission sometimes known as the "carrot," and the FOV never crossed the shock front (as delineated by the leading X-ray shell in the NW). This spectrum shows relatively strong 980 Å emission in comparison with the global spectrum of Figure 2a. Figure 5b is taken from the N portion of the Loop. Here the long axis of the FOV is oriented nearly perpendicular to the shock front, so we are seeing emission not only at the shock front but also from the region ∼6 pc behind it. However, the binning region for this spectrum is such that the FOV never crosses bright optical emission, so this spectrum should be representative of the northern X-ray shock front visible in Ku et al.'s (1984) map.
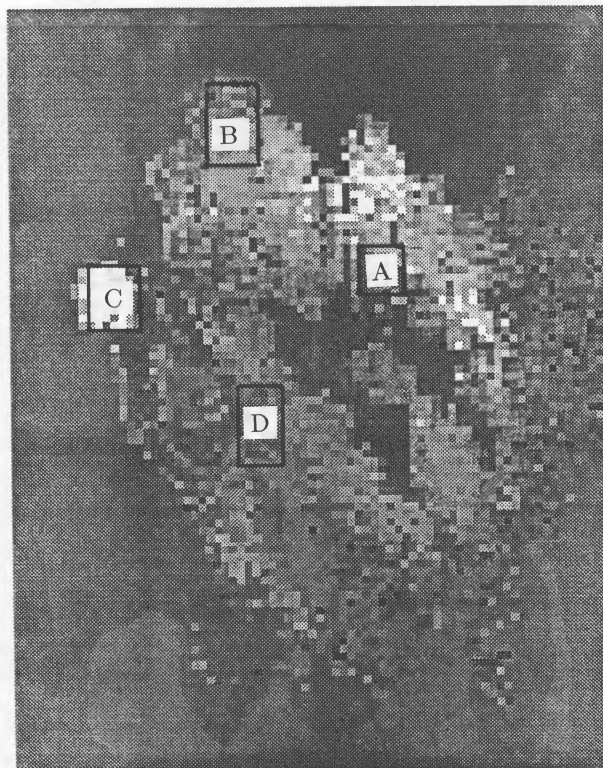
Here the 1035 Å peak is nearly twice as strong as the 980 Å feature. Figure 5c is a representative spectrum from the bright eastern edge of the Cygnus Loop including both the shock front and the bright optical filaments. This region is the brightest seen, but this is due in part to sampling effects. Figure 5d was taken from the SE area of the Loop, which comprises some of the lowest surface brightness emission. This region does not include either the shock front or any bright optical emission. While the surface brightness is quite low, it is only slightly fainter than the normalized global spectrum in Figure 2a, to which it otherwise looks very similar.

As mentioned previously, the *Voyager* FOV was oriented nearly parallel to the shock front in the NW and SE. Unfortunately, coverage did not quite extend out to the shock front in these regions, although it is very close in the NW. Because of the orientation of the slit in the NW, we can step inward from the edge of the remnant, maintaining as much spatial resolution as possible. Such a succession of spectra is shown in Figure 7. Coordinates for the binning areas are given in Table 2; the binning areas are shown superposed on the red POSS image in Figure 8 (Plate 8). The spectra are in order from near the NW limb (Fig. 7a) to the bright "carrot" region (Figs. 7d–7g). In Figure 7h the binning region has nearly passed through the "carrot" region toward the projected interior of the remnant. The observed ratio of the 1035 Å peak to the 980 Å peak starts out at ∼3, near the limb, systematically falls to less than 1, and then rises again to ∼1 as one steps inward.

The spectra shown in Figures 5 and 7 have been measured using the "splot" package in IRAF to determine flux centroids and widths of the two emission peaks used to create the maps.
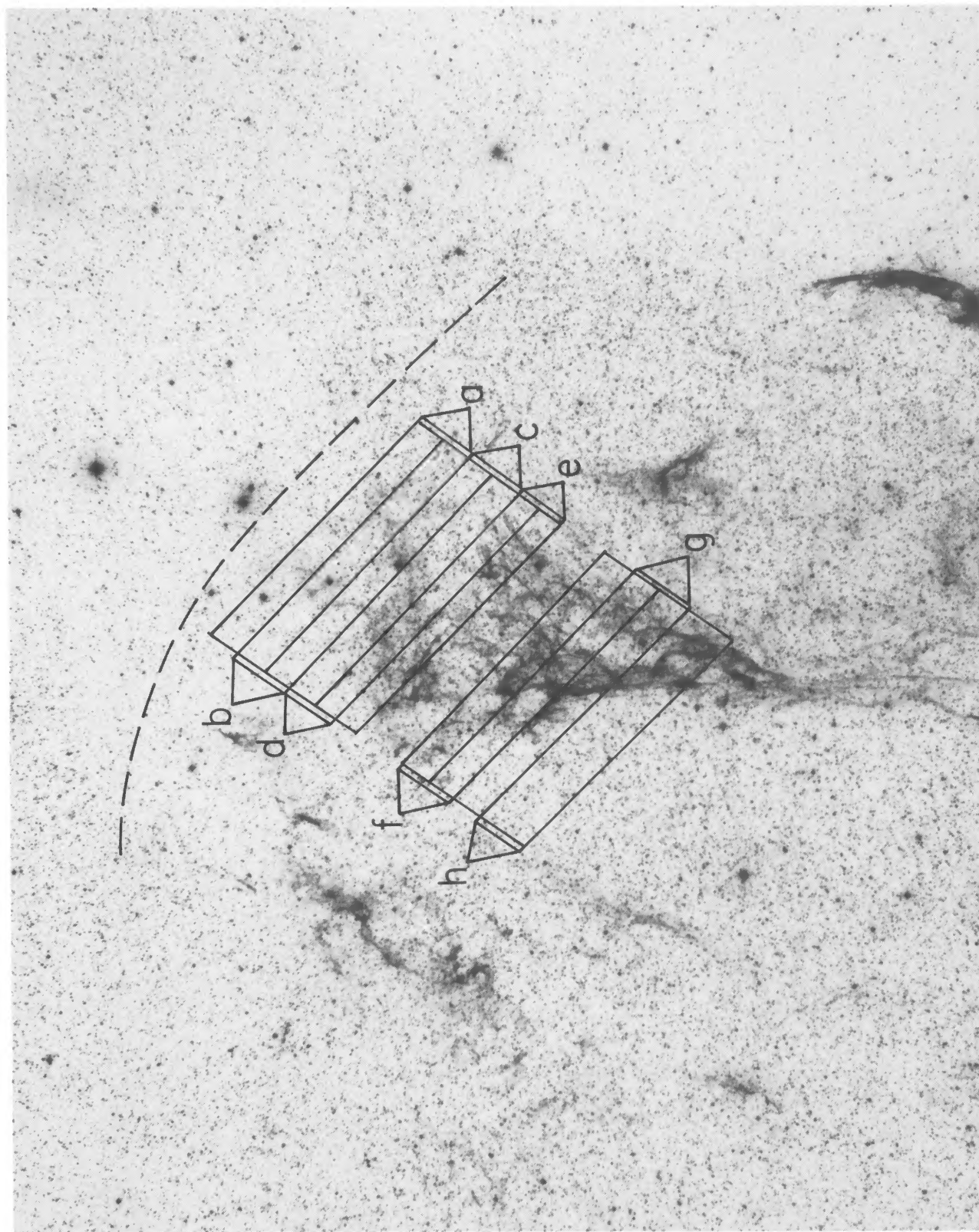
PLATE 6

FIG. 8.—Enlarged portion of the NW Cygnus Loop from the red Palomar print. The overlay shows regions extracted to produce the spectra in Fig. 7. Box furthest to the NW corresponds to Fig. 7a, and the box furthest to the SE corresponds to Fig. 7h. Primary shock front as delineated by the X-ray shell in the NW is highlighted with a dashed line.

BLAIR et al. (see 374, 206)

TABLE 2

COORDINATES FOR SPECTRAL EXTRACTION REGIONS

| Figure	R.A. (1950)	Decl. (1950)
5a	311°54	31°10
	311.54	31.40
	311.85	31.40
	311.85	31.10
5b	312.65	32.00
	312.65	32.50
	313.00	32.50
	313.00	32.00
5c	313.50	30.90
	313.50	31.30
	313.90	31.30
	313.90	30.90
5d	312.45	30.00
	312.45	30.50
	312.80	30.50
	312.80	30.00
7a	311.14	31.68
	311.54	32.03
	311.61	31.95
	311.21	31.60
7b	311.18	31.64
	311.58	31.99
	311.65	31.91
	311.25	31.56
7c	311.21	31.60
	311.61	31.95
	311.68	31.87
	311.28	31.52
7d	311.25	31.56
	311.65	31.91
	311.72	31.83
	311.32	31.48
7e	311.28	31.52
	311.68	31.87
	311.75	31.79
	311.35	31.44
7f	311.42	31.36
	311.82	31.71
	311.89	31.63
	311.49	31.28
7g	311.46	31.32
	311.86	31.67
	311.93	31.59
	311.53	31.24
7h	311.53	31.24
	311.93	31.59
	312.00	31.51
	311.60	31.16
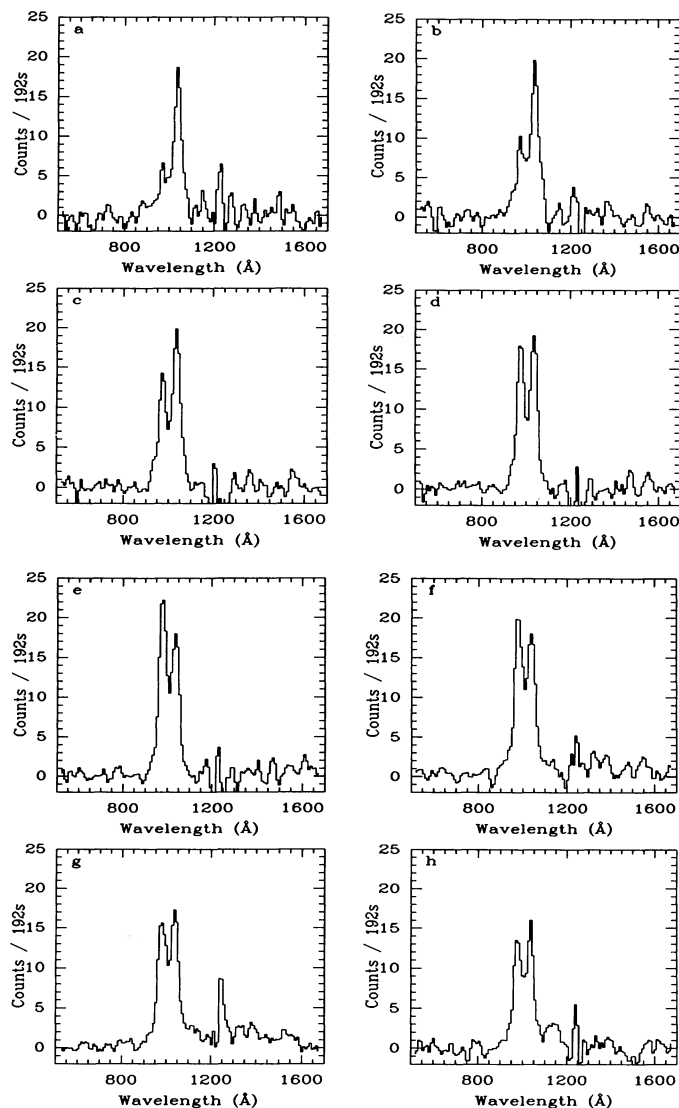
FIG. 7.—Spectra extracted from the regions indicated in Fig. 8, stepping in from the NW edge of the remnant through the bright optical "carrot" region. Vertical scaling is the same as in Fig. 5. Note the large relative strength of the 1035 Å feature at the shock front (a) and that this feature remains at nearly constant intensity throughout the series of spectra.

The "deblend" feature was used to fit Gaussian profiles (clearly only an approximation) to the features to derive this information. Almost invariably, the feature we have been calling the "1035 Å peak" is centered at 1036 ± 1 Å, and has a Gaussian FWHM of ~ 41 Å, somewhat wider than expected from a single line. The shorter wavelength peak is somewhat more variable both in central wavelength and width. In spectra where it is strong (such as Fig. 7e), the centroid is always near 978 Å, and the line has a Gaussian FWHM of ~ 38 Å (Again, somewhat high for a single line). As the 980 Å peak weakens (see Fig. 7a), the Gaussian fit broadens (FWMH ~ 45 Å) and shifts to the blue (~ 970 Å). The 1035:980 ratios from these Gaussian fits range only from ~ 0.6–3.0. However, the broadening of the 980 Å feature as it weakens could indicate blending with other lines.

4. DISCUSSION

The global spectrum in Figure 2a must contain a mixture of emission from radiative shocks, nonsteady flow shocks, and the nonradiative primary shock that corresponds to the X-ray edge of the SNR. Such a globally averaged spectrum of the Cygnus Loop has never been obtained before; it is useful to have such a spectrum to obtain an estimate of the total luminosity of the remnant in various emission features, as well as for comparison with extragalactic SNRs where the lower spatial resolution would cause the various types of emission, if present, to be blended together. The low spectral resolution in the *Voyager* data does not allow us to ascribe the emission seen in various emission peaks to a given emission line unambiguously. However, there are strong reasons to believe that the 980 Å feature is predominantly due to C III $\lambda 977$ and that the 1035 Å feature is primarily O VI $\lambda\lambda 1032$, 1038. Below we

first discuss the line identifications and then discuss the global spectrum.

Because there are so few existing observations in the sub–Lyα region, we turn to shock models to provide some guidance as to what lines are expected in this spectral region. Hartigan, Raymond, & Hartmann (1987, hereafter HRH) recently published a grid of radiative shock models varying the shock velocity from 20 to 400 km s⁻¹. Although calculated for use in interpreting the emission from bow shocks in Herbig-Haro objects, the densities in the "E" model series are low enough that the relative line intensities can be compared with SNR spectra (J. Raymond 1989, private communication). These models will be discussed in more depth below, but they show that C III λ977 and O VI λλ1032, 1038 are the dominant transitions expected in the 912–1200 Å region. There is a fairly sharp transition in relative intensities of these lines near ∼150 km s⁻¹; shocks in the 100–140 km s⁻¹ range have strong C III λ977 emission but do not have high enough postshock temperatures to produce O VI λλ1032, 1038. Shocks above 160 km s⁻¹ have very strong O VI emission with O VI:C III ratios ranging from ∼5.5–12. It is encouraging that the measured wavelengths of the two emission peaks seen in the *Voyager* spectra are close to those expected for the strongest calculated transitions.

It is possible to imagine that one or both of the main emission peaks in the *Voyager* spectra are comprised of several lines of varying ionization that could change intensity with position. Judging from the Gaussian line fits discussed above, this may affect the 980 Å peak and thus could also affect the appearance of the 980 Å map and the estimates of the C III line intensity. While C III λ977 is the only strong line expected near 980 Å, clearly other lines may contribute, especially as this peak gets weaker. The HRH models show N III λ991 at about 30% of the strength of C III and O VI near 160 km s⁻¹, but much weaker than the dominant line at other velocities. N III is closer in wavelength to C III than to O VI and is similar in ionization potential to C III. Hence N III would probably have a similar distribution to C III and O III and would not destroy the correlation seen in Figure 4. Any Lyβ (1025 Å) or higher Lyman series lines could also cause blending, but radiative transfer in the Lyman lines is uncertain, and these lines are not predicted in the shock models. No other lines are predicted that could compete with C III to comprise the 980 Å peak. We conclude, as did Shemansky et al. (1979), that C III is the dominant contributor to the 980 Å peak, especially when it is strong.

The identification of the 1035 Å peak is in principle more complicated, but in reality probably more straightforward. Shemansky et al. (1979) discussed possible identifications for this feature at some length, but none of the additional transitions discussed by them is expected to rival the strength of O VI. Shemansky et al. concluded that the 1035 Å feature was C II λ1037. Their rejection of O VI for the 1035 Å feature was based in part on the assumption that the temperatures in the UV-emitting regions were low compared with that needed to produce O VI. (Early results from *IUE*, for instance, seemed to be consistent with shock velocities of only ∼100 km s⁻¹; Benvenuti et al. 1980; Raymond et al. 1980). The similarity of our 1035 Å map with the X-ray data (as discussed earlier) argues against the C II interpretation and strengthens the identification of the 1035 Å peak with O VI.

There is further reason to believe that C II λ1037 does not contribute to the 1035 Å peak in a significant way. HRH tabu-

late C II λ1336 but do not show C II λ1037 in their tables. However, λ1037 was calculated in these models, and these data have been provided by P. Hartigan (1990, private communication); the 1037:1336 ratio is essentially constant at velocities above 100 km s⁻¹ at a value of 0.11. The absence of C II λ1336 from the global spectrum in Figure 2b (see below) makes it highly unlikely that C II λ1037 contributes significantly to the 1035 Å peak in the global Cygnus Loop spectrum. (We note that while the absence of C II λ1336 in the *IUE* spectra is often attributed to resonance scattering in edge-on shocks [see Raymond et al. 1981], this mechanism should not affect the line intensity in the global spectrum. Also, because of its lower oscillator strength, λ1037 would be less affected by this process than λ1336.) Given also the central wavelength and line width from the Gaussian line fits, we conclude that O VI λλ1032, 1038 is the most likely identification for the 1035 Å peak in the *Voyager* spectra.

With these line identifications, the spectra shown in Figure 7 can be understood as the following: the spectrum in Figure 7a mainly samples the primary nonradiative shock front, but more and more radiative shock emission mixes in as one steps into and through the carrot region. However, notice that the intensity of the 1035 Å peak remains nearly constant through this progression. This would argue against any enhancement of O VI emission in the regions of bright optical emission, as would be the case if evaporation of clouds was significant in these regions.

Taken at face value, assuming the peaks in the *Voyager* spectra are dominated by C III and O VI, the range of observed 1035:980 ratios in the *Voyager* data (∼0.6–3 from the Gaussian fits) are only compatible with a narrow velocity range of ∼160–180 km s⁻¹ in the radiative models. (This shock velocity is in excellent agreement with the shock velocity estimated by RBFG for a position on the NE nonradiative shock front.) However, this simple comparison is probably not valid for two reasons. First, because of projection effects, the blending of radiative and nonradiative emission within the large *Voyager* FOV and/or the blending of shocks with different velocities would clearly tend to confuse any direct comparison with radiative models. While there is no similar grid of nonradiative shock models available, nonradiative shocks are expected to have stronger high-ionization lines (such as O VI) and weaker low-ionization lines (such as C III) in comparison with radiative shock models of the same velocity (see RBFG). Second, the observed range in the 1035:980 ratio is probably an underestimate of the true range of variation in O VI:C III. As mentioned earlier, the blending of additional faint spectral lines may become significant as the 980 Å peak becomes weaker. Hence, the Gaussian fits would overestimate the strength of the C III line and thus underestimate the range of variation in the ratio.

In Figure 2b we show the global Cygnus Loop spectrum after applying the nominal *Voyager* flux calibration (Holberg et al. 1982). The features or potential features seen at ≥1200 Å are more uncertain because of *Voyager*'s low sensitivity in this region, but this representation places the sub-Lyα emission in its proper context to other emissions seen by *IUE*. While some of the weaker features may be questionable, clearly the peak at 1550 Å is real and due to C IV. The peak at ∼1650 Å may be due to a blend of He II λ1640 and O III] λ1663. However, this feature appears anomalously narrow given the wavelength separation of these lines and the *Voyager* spectral resolution.

In Table 3 we show calculated values of the average

TABLE 3

CYGNUS LOOP SURFACE BRIGHTNESS MEASUREMENTS

	EMISSION FEATURE		
PARAMETER	980 Å	1035 Å	1550 Å
Average observed surface brightness:			
B_0 (ergs cm^{-2} s^{-1} sr^{-1})	4.0×10^{-6}	8.8×10^{-6}	8.9×10^{-6}
B_0 (photons cm^{-2} s^{-1} sr^{-1})	2.0×10^5	4.4×10^5	7.0×10^5
B_0 (rayleighs)	2.5	5.7	8.5
Average dereddened[a] surface brightness:			
B_i (ergs cm^{-2} s^{-1} sr^{-1})	1.2×10^{-5}	2.2×10^{-5}	1.9×10^{-5}
B_i (photons cm^{-2} s^{-1} sr^{-1})	6.0×10^5	1.1×10^6	1.5×10^6
B_i (rayleighs)	7.5	14.3	18.3
Peak observed[b] surface brightness:			
B_0 (ergs cm^{-2} s^{-1} sr^{-1})	1.5×10^{-5}	2.6×10^{-5}	...[c]
B_0 (photons cm^{-2} s^{-1} sr^{-1})	7.4×10^5	1.3×10^6	...
B_0 (rayleighs)	9.3	16.9	...
Peak dereddened[a,b] surface brightness:			
B_i (ergs cm^{-2} s^{-1} sr^{-1})	4.7×10^{-5}	6.2×10^{-5}	...[c]
B_i (photons cm^{-2} s^{-1} sr^{-1})	2.3×10^6	3.1×10^6	...
B_i (rayleighs)	28.9	40.3	...

[a] Reddening correction assumes a Seaton 1979 curve. Slight extrapolation was necessary to correct the 980 Å feature.

[b] Spectrum shown in Fig. 5c was used to estimate peak surface brightnesses.

[c] 1550 Å feature not measurable in peak spectrum.

observed surface brightnesses of the C III, O VI, and C IV features derived from the global spectrum in Figure 2b, and from the highest observed surface brightness region (utilizing the spectrum of the bright eastern region from Figure 5c). The reddening correction was made assuming a Seaton (1979) extinction curve and $E(B-V) = 0.08$. (A slight extrapolation is necessary to correct the C III line.) These data indicate that the global surface brightnesses of C III, C IV, and O VI are similar to each other (within a factor of 2).

The total flux in the 980, 1035, and 1550 Å features in the Cygnus Loop can be determined from the Voyager data in various ways. The most straightforward approach, which we have adopted here, is simply to sum the surface brightness in the global spectra and correct for the "holes" in coverage created by our binning method. The renormalization for the exposure map depends somewhat on the actual distribution of surface brightness in the SNR. In order to estimate this renormalization factor, we have compared the total flux in the raw X-ray image to the flux in the X-ray image after it has been smoothed and convolved with the time coverage map (which, as we have indicated previously, is what created the "holes"). The summed flux in the smoothed, convolved X-ray image is 66% of that in the raw X-ray image which requires a renormalization factor of ~1.5. (We have also carried out this exercise for the [O III] image; in that case the smoothed map contains 60% of the total intensity, but these data from photographic plates may not be entirely linear in response.) Thus from the raw fluxes in the total, calibrated, and dereddened spectra, 2.5×10^{-8} and 4.2×10^{-8} ergs cm^{-2} s^{-1} in the 980 and 1035 Å peaks, we infer corrected fluxes of 3.8×10^{-8} and 6.4×10^{-8} ergs cm^{-2} s^{-1} and luminosities of 2.7×10^{36} and 4.6×10^{36} ergs s^{-1}. The total luminosity in the 900–1200 Å range of $\sim 7 \times 10^{36}$ ergs s^{-1} is considerably larger than the total 0.1–4 keV X-ray luminosity of 1.1×10^{36} ergs s^{-1} (Ku et al. 1984). The feature we have identified with C IV λ1550 has an apparent flux which exceeds both O VI and C III, and a total

luminosity of roughly 4.0×10^{36} ergs s^{-1}. Even though these numbers are uncertain, they are the first and only estimates of the total UV luminosity of the Cygnus Loop.

Since the Voyager aperture is so large it is likely that any spectrum obtained of the Cygnus Loop will sample a variety of shock conditions. As a result, we would not expect the Voyager spectra to be well fitted by a single shock model. The fact that the C III and O VI emissions are distributed differently is just one example of this situation.

It is nevertheless useful to compare the spectra we have obtained with shock models such as those of HRH. In the context of these models a substantial portion of the O VI must be arising from shocks with velocities in excess of 160 km s^{-1} since the surface brightness of O VI exceeds that of C IV. Furthermore, since the ratio of O VI to Hα or [O III] is large, these shocks will not be bright in the optical even if they have fully developed cooling and recombination zones. For example, for a 200 km s^{-1} shock the O VI surface brightness will be 24 (20) times brighter than the Hα ([O III] λ5007) surface brightness. Thus the expected Hα surface brightness based on an O VI surface brightness of 2.2×10^{-5} ergs cm^{-2} s^{-1} sr^{-1} ($= 5 \times 10^{-16}$ ergs cm^{-2} s^{-1} arcsec^{-2}) would be just 9×10^{-7} ergs cm^{-2} s^{-1} sr^{-1} ($= 2 \times 10^{-17}$ ergs cm^{-2} s^{-1} arcsec^{-2}).

A more extreme possibility is that we are seeing a higher velocity example of the nonsteady flow phenomenon, whereby a recent shock has not had time to develop a full cooling and recombination zone and thus shows enhanced high-ionization line intensities. RBFG have demonstrated the presence of 170–200 km s^{-1} shocks in the northeast Cygnus Loop and Hester & Raymond (1987) have even found evidence for nonsteady flow [O III] filaments in the same region. RBFG also estimated a low preshock neutral fraction at the position they observed, and the lower Hα surface brightnesses of other adjacent edge-on filaments could indicate conditions even closer to full preionization. It is encouraging to this idea that the fully preionized 160 and 180 km s^{-1} models of HRH show

C III:O VI:C IV ratios similar to the *Voyager* global and peak data shown in Table 3.

In actuality it is not clear whether radiative or nonradiative shock models are more applicable to the case of O VI emission in the Cygnus Loop. For a density of 1 cm^{-3} the thickness of the shock (as measured by the distance from the shock front to the point where the plasma temperature returns to 10^4 [10^3] K) is 0.15 (0.16) pc for a 200 km s^{-1} shock. (The thickness scales inversely as the shock density.) For a 400 km s^{-1} radiative shock and a density of 1 cm^{-3}, the thickness is 3.6 pc.

In fact, for the shock speeds being discussed there is no sharp boundary between the ionization and recombination zones for ions such as O^{+5} and Ne^{+4}. The RBFG observation of a bright nonradiative filament on the NE limb of the Cygnus Loop could be fitted with a ~ 200 km s^{-1} shock encountering a plasma with a density of 1–3 cm^{-3}. RBFG noted that if this shock model were correct, one would also expect O VI emission with a surface brightness of 1.2×10^{-6}–1.2×10^{-5} ergs cm^{-2} s^{-1} sr^{-1}, depending on whether electrons and ions in the postshock gas equilibrate rapidly (e.g., plasma turbulence) or more slowly (through Coulomb collisions). The particular shock model chosen by RBFG does not explain the emission we see largely because the ratio of O VI emission to C IV emission is too low; this is most likely due to the fact that the shock was truncated at an age of 360 yr for the rapid equilibration case and 455 yr for the Coulomb equilibration case in order to match the strength of [Ne V] $\lambda 3426$. Preliminary runs of a revised version of the code used by RBFG indicate that much stronger O VI emission is possible from nonradiative shocks when the models are not truncated as early. These models also indicate that as much as one-third to one-half of the O VI emission we see could arise in 400 km s^{-1} shocks of the kind needed to explain the X-ray emission (see Ku et al. 1984). These models will be discussed in a future paper.

The strength of C III $\lambda 977$ and O VI $\lambda\lambda 1032$, 1038 is a measure of the amount of material at temperatures of 1–3×10^5 K. A crude estimate of the amount of material at these temperatures can be obtained as follows. Assume that an emission-line strength, such as O VI $\lambda\lambda 1032$, 1038, is created predominantly in a plasma which is close to collisional equilibrium and has a temperature T_{O+5} such that the emissivity $\Lambda_{O\,VI}$ in the line is maximized. The minimum volume emission measure, $EM_{O\,VI}$, required to produce the observed line luminosity is then given by

$$EM_{O\,VI} = \frac{L_{O\,VI}}{\Lambda_{O\,VI}},$$

where $L_{O\,VI}$ is the luminosity in O VI $\lambda\lambda 1032$, 1038. Assume the interior of the SNR is in rough pressure equilibrium, in which case the density in the O^{+5} zone is given by

$$n_{O+5} = \frac{T_X}{T_{O+5}} n_X,$$

where n_X and T_X are the density and temperature of the X-ray gas. Then the mass of O VI emitting gas is given approximately by

$$M_{O\,VI} \approx \frac{n_X}{n_{O+5}} \frac{EM_{O\,VI}}{EM_X} M_X,$$

where M_X is the mass of X-ray–emitting material. Using an updated version of Raymond & Smith's (1976) thin plasma code, we find a peak emissivity of $\sim 1.3 \times 10^{-22}$ ergs s^{-1} cm^3 at a temperature of $\sim 10^5$ K for C III $\lambda 977$ and a peak emissivity of $\sim 9.3 \times 10^{-23}$ ergs s^{-1} cm^3 at a temperature of 3×10^5 K for O VI. On the other hand, the soft X-ray emissivity of a middle-aged SNR will be $\sim 10^{-22}$ ergs s^{-1} cm^3 after allowing for nonequilibrium effects (see Hamilton, Sarazin, & Chevalier 1983). The volume emission measures required to explain the C III, O VI, and X-ray emission are therefore 2.1×10^{58} cm^{-3}, 4.9×10^{58} cm^{-3}, and 1.1×10^{58} cm^{-3}. Given a radius of ~ 19 pc and assuming a filling factor of 0.25 for the X-ray gas, we infer a hydrogen density of the X-ray–emitting gas n_X of 0.21 cm^{-3} and a total mass of the X-ray gas of 49 $M_\odot$. (Note: these estimates are somewhat lower than derived by Ku et al. 1984; presumably they assumed a lower emissivity.) Taking the X-ray temperature to be 3×10^6 K, this implies densities of 6.3 cm^{-3} and 2.1 cm^{-3} in the C^{+2} and O^{+5} zones. The masses required to generate the observed C III $\lambda 977$ and O VI $\lambda\lambda 1032$, 1038 lines are $\sim 6\%$ and $\sim 45\%$ of the mass required to produce the X-ray emission. The thermal energy content of the gas associated with C III and O VI is $\sim 0.2\%$ and $\sim 4.5\%$ of that of the X-ray gas. This is consistent with the hypothesis that the 1035 Å peak is dominated by O VI since the O VI should be more closely associated with the X-ray gas.

5. SUMMARY AND FUTURE WORK

We have used data obtained with the UVS on board *Voyager 2* to create maps of the Cygnus Loop at 980 and 1035 Å and compare with X-ray and optical data. We have also extracted sample spectra in the 500–1700 Å range from various positions in the Cygnus Loop to study variations in both relative and absolute line intensities. Both peaks are seen throughout the Cygnus Loop, and while part of this may be due to blending of radiative and nonradiative emission in the large FOV, both emissions are intrinsically widespread in the Cygnus Loop. We believe the 980 Å feature is mainly due to C III $\lambda 977$ and the 1035 Å feature is mainly due to O VI $\lambda\lambda 1032$, 1038. We estimate the total absolute luminosity of O VI $\lambda\lambda 1032$, 1038 to be 4.6×10^{36} ergs s^{-1}, and that of the C III $\lambda 977$ to be 2.7×10^{36} ergs s^{-1}, making these emissions several times brighter than the 0.1–4 keV X-ray luminosity of the Cygnus Loop. The peak O VI surface brightnesses immediately behind the shock front in the N and NW regions and the high average O VI surface brightness both lead us to believe that shocks with velocities ≥ 160 km s^{-1} are widespread in the Cygnus Loop.

A large additional set of *Voyager* UVS data on the northeast Cygnus Loop has yet to be analyzed. These data will be particularly important for studying the NE nonradiative primary shock since they were taken when the long dimension of the FOV was parallel to the shock front in this region. Model calculations will be convolved with the *Voyager* resolution and fitted to *Voyager* spectra to better understand the emission-line content and variations in the spectra. We also look forward to analyzing two Cygnus Loop observations that were made with the Hopkins Ultraviolet Telescope (HUT) when it flew on the space shuttle in 1990 December as part of the Astro-1 mission (Blair & Gull 1990). HUT observed the 850–1850 Å region with ~ 3 Å resolution. Analysis of these data will give us our first detailed look at the SNR emissions in the sub–Lyα region.

REFERENCES

Benvenuti, P., Dopita, M., & D'Odorico, S. 1980, ApJ, 238, 613
Blair, W. P., & Gull, T. R. 1990 S&T, 79, 591
Boulares, A., & Cox, D. P. 1988, ApJ, 333, 198
Braun, R., & Strom, R. G. 1986, A&A, 164, 193
Broadfoot, A. L., et al. 1977, Space Sci. Rev., 21, 183
———. 1981, J. Geophys. Res., 86, 8259
Carruthers, G. R., & Page, T. 1976, ApJ, 205, 397
Charles, P. A., Kahn, S. M., & McKee, C. F. 1985, ApJ, 295, 456
Chevalier, R. A., Kirshner, R. P., & Raymond, J. C. 1980, ApJ, 235, 186
Cox, D. P., & Raymond, J. C. 1985, ApJ, 298, 651
Dopita, M. A., Binette, L., D'Odorico, S., & Benvenuti, P. 1984, ApJ, 276, 653
Fesen, R. A., Blair, W. P., & Kirshner, R. P. 1982, ApJ, 262, 171
Fesen, R. A., & Itoh, H. 1985, ApJ, 295, 43
Hamilton, A. J. S., Sarazin, C., & Chevalier, R. A. 1983, ApJS, 51, 115
Hartigan, P., Raymond, J., & Hartmann, L. 1987, ApJ, 316 323 (HRH)
Hester, J. J., & Cox, D. P. 1986, ApJ, 300, 675
Hester, J. J., Parker, R. A. R., & Dufour, R. J. 1983, ApJ, 273, 219
Hester, J. J., & Raymond, J. C. 1987, in IAU Colloquium 101, Supernova Remnants and the Interstellar Medium, ed. R. S. Roger & T. L. Landecker (Cambridge: Cambridge University Press), 415
Hester, J. J., Raymond, J. C., & Danielson, G. 1986, ApJ, 303, L17
Holberg, J. B. 1986, ApJ, 311, 969
———. 1991, in IAU Colloquium 123, Observations in Earth Orbit and Beyond, ed. Y. Kondo (Dordrecht: Kluwer), in press
Holberg, J. B., Forrester, W. T., Shemansky, D. E., & Barry, O. C. 1982, ApJ, 257, 656
Jenkins, E. B., Silk, J., & Wallerstein, G. 1976, ApJS, 32, 681

Keen, N. J., Wilson, W. E., Haslam, C. G. T., Graham, D. A., & Thomasson, P. 1973, A&A, 28, 197
Kirshner, R. P., & Taylor, K. 1976, ApJ, 208, L83
Ku, W. H.-M., Kahn, S. M., Pisarski, R., & Long, K. S. 1984, ApJ, 278, 615
McKee, C. F., Cowie, L. L., & Ostriker, J. P. 1978, ApJ, 219, L23
McKee, C. F., & Hollenbach, D. J. 1980, ARA&A, 18, 615
McKee, C. F., & Ostriker, J. P. 1977, ApJ, 218, 148
Miller, J. M. 1974, ApJ, 189, 239
Parker, R. A. R., Gull, T. R., & Kirshner, R. P. 1979, An Emission-Line Survey of the Milky Way (NASA SP-434) (Washington: GPO)
Raymond, J. C., Black, J. H., Dupree, A. K., Hartmann, L., & Wolff, R. S. 1980, ApJ, 238, 881
———. 1981, ApJ, 246, 100
Raymond, J. C., Blair, W. P., Fesen, R. A., & Gull, T. R. 1983, ApJ, 275, 636 (RBFG)
Raymond, J. C., Hester, J. J., Cox, D. P., Blair, W. P., Fesen, R. A., & Gull, T. R. 1988, ApJ, 324, 896
Raymond, J .C., & Smith, B. W. 1977, ApJS, 35, 419
Sakhibov, F. K., & Smirnov, M. A. 1983, Soviet Astr., 27, 395
Seaton, M. J. 1979, MNRAS, 187, 73P
Seward, F. 1990, ApJS, 73, 781
Shemansky, D. E., Sandel, B. R., & Broadfoot, A. L. 1979, ApJ, 231, 35
Shemansky, D. E., Judge, D. L., & Jessen, J. M. 1984, in IAU Colloquium 81, The Local Interstellar Medium, ed. Y. Kondo, F. C. Bruhweiler, & B. D. Savage (NASA CP-2345), 24
Teske, R. G. 1990, ApJ, 365, 256